PHOTONICS Research

Inverse-designed photonic crystals for tailored OAM beam generation and multiplexing in momentum space

Ruhuan Deng,[1] Tongyu Li,[1] Wenzhe Liu,[1,2,3,4] Jiajun Wang,[1,3,4,6] Lei Shi,[1,2,3,4,5,7] and Jian Zi[1,2,3,4,5]

[1]State Key Laboratory of Surface Physics Key Laboratory of Micro- and Nano-Photonic Structures (Ministry of Education) and Department of Physics, Fudan University, Shanghai 200433, China
[2]Institute for Nanoelectronic Devices and Quantum Computing, Fudan University, Shanghai 200438, China
[3]Shanghai Research Center for Quantum Sciences, Shanghai 201315, China
[4]Shanghai Key Laboratory of Metasurfaces for Light Manipulation, Fudan University, Shanghai 200433, China
[5]Collaborative Innovation Center of Advanced Microstructures, Nanjing University, Nanjing 210093, China
[6]e-mail: jiajunwang@fudan.edu.cn
[7]e-mail: lshi@fudan.edu.cn

Received 21 October 2025; revised 13 November 2025; accepted 18 November 2025; posted 19 November 2025 (Doc. ID 582279); published 27 February 2026

The generation of optical vortex beams with varying orbital angular momentum (OAM) beam is crucial across diverse fields, including optical communication, topological photonics, and quantum optics, among others. Recently, photonic crystals (PhCs) have emerged as a powerful platform for generating vortex beams in momentum space, offering significant advantages such as the absence of a geometric center for alignment. However, modifications to the unit cell of a PhC slab can substantially alter its overall momentum-space properties, making it particularly challenging to realize the desired vortex beams and their multiplexing. Here, we present an inverse design framework for PhCs that enables precise generation of vortex beams with tailored properties. We demonstrate the generation of vortex beams with specific OAM orders through PhCs and further achieve polarization-division and momentum-space-division multiplexing. This study highlights the potential of PhCs for generating vortex beams with diverse orders and multiplexing schemes. In addition, it expands their functionality in practical applications and offers a new platform to explore their rich topological phenomena.

https://doi.org/10.1364/PRJ.582279

1. INTRODUCTION

An optical vortex beam is characterized by a helical phase front and a central phase singularity with vanishing intensity [1]. It can carry different topological charges, which correspond to the orbital angular momentum (OAM) order, defined as the number of 2π phase windings around the beam axis in the form $e^{il\theta}$ (θ is the azimuthal angle and l is the topological charge). This distinctive feature, as an additional degree of freedom, has enabled versatile control of light and has led to widespread applications in optical communication [2,3], imaging [4,5], and quantum information processing [6,7]. Building on these advances, generating optical vortex beams with specific OAMs and tailored properties continues to attract significant interest for both advanced applications and fundamental research [8–10].

Optical vortex beams are typically generated through real-space light manipulation [11] using spatial light modulators [12], phase plates [13,14], and metasurfaces [15,16]. These methods rely on high-precision alignment in real space. Recently, PhCs have emerged as a potential platform for vortex beam generation [17–19]. Their periodic real-space structures can generate vortex beams in momentum space, offering significant advantages, including the elimination of geometric center alignment requirements. Modifications to any part of a PhC's unit cell affect transmissions across the entire momentum-space spectrum (i.e., at different angles) simultaneously. This characteristic makes momentum-space design for OAM beam generation extremely challenging, as the whole spectrum requires simultaneous consideration. To date, PhC designs for vortex beam generation rely largely on physical intuition based on topological polarization vortices and remain restricted to simple geometries with high symmetry [18,19]. These limitations severely constrain the OAM orders of generated vortex beams and hinder arbitrary modulation capabilities, preventing further multiplexing functionalities.

Inverse design, a powerful and increasingly adopted methodology, provides a possible approach for momentum space design [20,21]. By leveraging algorithms such as adjoint method

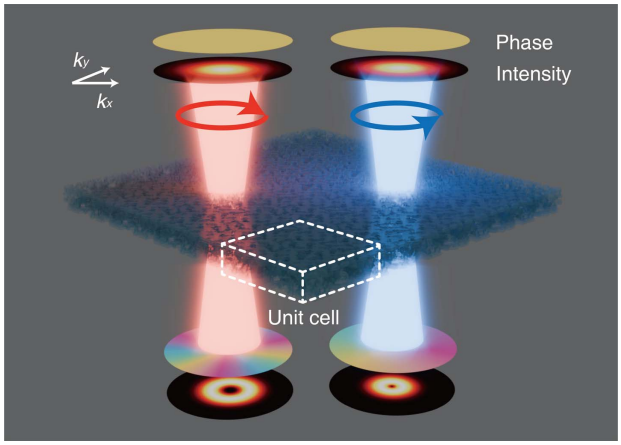

Fig. 1. Schematic diagram of the inverse-designed multiplexed PhC for generating OAM beams with tailored properties. The inverse-designed PhC can generate −1 order vortex beam for an LCP incident Gaussian beam and generate −3 order vortex beam for an RCP incident Gaussian beam at the same wavelength.

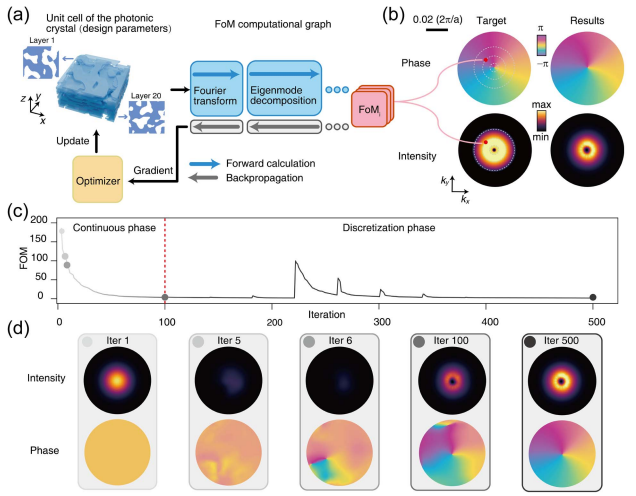

Fig. 2. Inverse design method and the optimization result for −1 order OAM beam generation. (a) Schematic of the optimization procedure. RCWA is used to simulate the field and calculate the FoM, backpropagation is used to efficiently obtain the gradient, and an optimizer is used to update the design parameters based on the gradient. (b) Optimization target and results for the −1 order OAM beam generation. Red dot shows an example of FoM_i that composed the final FoM. (c) Evolution of the final FOM during the optimization process. (d) Phase and intensity profiles at specific iteration steps during the optimization.

[22], backpropagation [23], and machine learning [24], it enables the automatic optimization of device geometries to meet complex design objectives. With this framework, we are able to optimize transmission coefficients at different angles simultaneously and to make it possible to obtain satisfactory results. In PhCs, inverse design has been applied for tasks such as optical differentiation [25], polarization control [26], and bandgap design [27]. Until now, its application to the generation of optical vortex beams remains unexplored.

In this work, we present inverse-designed PhCs that can efficiently generate optical vortex beams with precisely tailored OAM orders exhibiting both spin and angle dependencies. By employing topology optimization through backpropagation in combination with the L-BFGS-B algorithm, this approach enables the discovery of complex PhCs and correspondingly intricate band structures, yielding unprecedented, high-performance PhCs that generate vortex beams with designed properties. To begin with, we successfully generate diverse OAM beams near the Γ point in momentum space, with both even and odd OAM orders. Furthermore, we achieve multiplexed vortex beam generation across different polarizations and momentum-space positions. A representative result is shown in Fig. 1. When illuminated with a left-handed circularly polarized (LCP) Gaussian beam, the inverse-designed PhC produces a co-polarized vortex beam of −1 OAM order near the Γ point. Switching the input light to right-handed circularly polarized (RCP) changes the output light to a −3 OAM order vortex beam also near the Γ point. Both multiplexed vortex beam generations exhibit remarkable efficiency, with near unity transmittance. Our approach significantly expands the functional capabilities of PhCs and underscores the powerful potential of inverse design methodologies in the OAM beam generation.

2. RESULTS

A. Topology Optimization with Backpropagation

Introducing additional design degrees of freedom in PhC unit cells enables the realization of more advanced and complex functionalities. To exploit this potential, we build a topology optimization framework based on backpropagation for the vortex beam generation, with the procedure shown in Fig. 2(a). Beginning with the unit cell structure of a PhC, the program first simulates its electromagnetic fields and evaluates the figure of merit (FoM) according to the design target. The gradients of the FoM with respect to the design parameters are then computed efficiently and automatically through backpropagation. These gradients are subsequently passed to the optimizer, which determines the direction and magnitude of parameter updates based on the optimization algorithm. This iterative procedure continues until the FoM converges to a satisfactory value, producing an optimized design.

In our formulation, topology optimization treats the unit cell of multilayer PhCs as a collection of small voxels, with their dielectric constants serving as the optimization parameters [28]. For fabrication feasibility, the dielectric constant of the structure is constrained to vary between 1 and 3 during optimization. Initially, ϵ is allowed to evolve continuously within this range, after which filter-and-threshold procedures are applied to discretize the structure for practical implementation [29]. Detailed configurations of each layer used in the optimization are provided in Appendix A. By systematically exploring this vast design space, our method enables the discovery of unprecedented high-performance designs.

The large number of design degrees of freedom makes the optimization problem highly challenging. To address this, we adopt the gradient-based optimizer L-BFGS-B in conjunction with backpropagation, which provides accurate gradients that guide the optimization efficiently through the high-dimensional parameter space. Backpropagation, originally

developed in mathematics and now widely used in computer science and deep learning, is a reverse-mode automatic differentiation technique that efficiently computes gradients for functions with many inputs and few outputs [30]. This is particularly well suited to our inverse design problem, which involves thousands of design parameters but only a few FoMs. Importantly, backpropagation requires only one forward simulation to compute all gradients, in contrast to the thousands of simulations needed for direct differentiation.

To realize this capability, all operations in the FoM calculation are implemented by the autograd module, which supports automatic differentiation through backpropagation [31]. During the computation, the computational graph is constructed, and each operation in the graph (like Fourier transform, drawn as blue blocks) is paired with a corresponding operation used to calculate the forward operation's vector-Jacobian product (drawn as gray blocks). After the forward pass, backpropagation is triggered and the gradient of the FoM with respect to design parameters is efficiently computed through the chain rule. For efficient simulation and optimization, we employ the rigorous coupled wave analysis (RCWA) algorithm to calculate electromagnetic fields, which is well-suited and computationally efficient for periodic structures such as photonic crystals. Specifically, we use GRCWA, an open-source implementation of RCWA that supports backpropagation, serving as the simulation kernel [32]. The resulting gradients are then supplied to the L-BFGS-B optimizer, which approximates the inverse Hessian and performs efficient updates while handling bound constraints on the variables [33]. Because gradient information is explicitly incorporated, this algorithm typically converges faster and requires fewer iterations.

To generate vortex beams with the desired properties, we need to precisely design the transmission coefficients of the PhC at different angles in momentum space. Both intensity and phase are considered simultaneously by defining FoMs as the Euclidean distance between the current and target transmission coefficients in complex space,

$$\mathrm{FoM}_i = |A_{\mathrm{current}} \cdot e^{i\phi_{\mathrm{current}}} - A_{\mathrm{target}} \cdot e^{i\phi_{\mathrm{target}}}|.$$

Here, A denotes the amplitude, and ϕ the phase of the transmission coefficient. This formulation inherently balances the contributions of intensity and phase while naturally accounting for the cyclic nature of the phase [25]. To facilitate smoother optimization, the transmission phase near the Γ point of the initial structure is set as the reference. Since the phase varies more rapidly near the singularity, we adopt a concentric-circle sampling scheme. This approach increases the sampling density close to the singularity with a limited number of points and can provide uniform angular sampling frequency. For vortex beams with different OAM orders and angles, sampling points are distributed along concentric circles centered at the target position. This strategy specifies vortex beam properties with fewer sampling points than uniform sampling, thereby accelerating the optimization process. The individual FoM_i values are then combined into the final FoM using the L2 norm, $\mathrm{FoM} = (\sum \mathrm{FoM}_i^2)^{1/2}$. It not only improves the differentiability and smoothness of the final objective function but also prevents domination by a few sampling points' FoM_i [30]. This balance is crucial, as the OAM order is a global property determined by all the sampling points in momentum space.

In previous studies, momentum-space OAM beams have typically been generated through geometric phases arising from topological polarization vortices under cross-polarization [17,18]. As an example to demonstrate the versatility of our inverse design approach, we optimize a co-polarized vortex beam with an OAM order of −1 near the Γ point, under LCP incident light at 780 nm. The target and optimized phase and intensity profiles are shown in Fig. 2(b). Sampling points are indicated by dashed lines, with a red dot marking one representative. From our experiment, a sampling step of 0.6 rad per point proves sufficient to generate smooth phase profiles and avoids unwanted low transmission due to abrupt phase changes. To further demonstrate the generality of our method, we also optimized OAM beams under cross-polarization, as presented in Appendix B.

The optimization successfully produces a pure −1 OAM order vortex beam with high transmission, as the optimized result closely matches the target. Figure 2(c) shows the evolution of the FoM, which decreases from 174.3 to 2.4 under 500 iterations (90 sampling points), and the whole optimization takes approximately 72 h on our server [Intel(R) Xeon(R) Gold 6248R CPU@3 GHz, 24 cores, 512 GB RAM]. After the first 100 iterations of free evolution, the optimization proceeds into the discretization phase. In this stage, spiky peaks appear in the FoM curve whenever discretization is enforced, reflecting abrupt structural adjustments introduced by binarization. Figure 2(d) illustrates the phase and intensity profiles at selected iteration steps, as indicated by the colored dots on the optimization curve. Interestingly, we observe that in the early stage, the optimization naturally prioritizes phase formation over intensity. The intensity initially decreases nearly to 0, which—although contrary to the requirement for high transmission—is advantageous for forming the phase singularity, as it necessarily coincides with vanishing intensity. Once the −1 OAM order phase singularity is established, the optimization subsequently increases the transmission efficiency and fine-tunes the phase profile and its position. This observation suggests that a multiphase optimization strategy may be advantageous for more demanding vortex beam designs since the competition between achieving high efficiency and establishing the singular phase profile is most acute in the initial stage of optimization.

B. Inverse Design PhCs for Vortex Beam Generation with Tailored Orders

To demonstrate the capability of our inverse design program in generating vortex beams with tailored OAM orders, we optimize PhCs to produce −1 and −2 OAM order vortex beams at a wavelength of 780 nm. Achieving high-quality vortex beams with both even and odd OAM orders remains particularly challenging for PhCs [19]. Conventional design methods rely on momentum-space polarization vortices and simple, high-symmetry geometries, where the generated beam's OAM order follows $l = \pm 2q$, with q denoting the topological charge of the polarization vortex. Most reported works have primarily focused on producing even-order OAM beams [17,18]. Odd-order OAM beams can, in principle, be realized

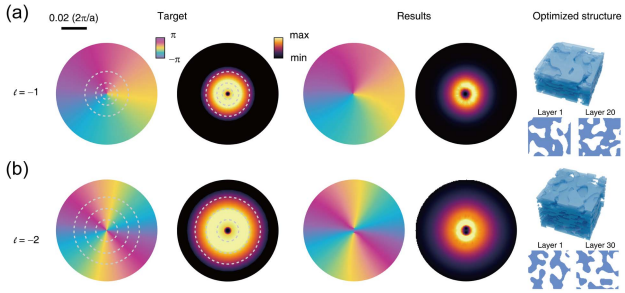

Fig. 3. Inverse-designed vortex beam with different orders. (a) The optimization target and results for the −1 order OAM vortex beam. (b) The optimization target and results for the −2 order OAM vortex beam.

by utilizing half charges around circular polarization points, but the achievable OAM orders remain limited [34].

In our design, we consider a square lattice with lattice constant a. Based on previous studies, larger lattice constants relative to the wavelength tend to yield better optimization results [25]. Accordingly, we set $a = 1500$ nm and a grid resolution of 15 nm. No symmetry constraints are imposed on the structure, allowing the generation of vortex beams with arbitrary OAM order [35].

The optimization results, shown in Fig. 3, confirm that vortex beams of both even and odd orders can be generated with high efficiency and purity. The phase and intensity profiles, as well as the locations of singular points, match the design requirements very well. A detailed analysis of the field distributions under cross-polarization and mode purity is provided in Appendices C and D. Dashed concentric circles on the target profiles indicate sampling points used to construct the FoM. For the −2 OAM order vortex beam, we increase the circle radii to ensure a physically appropriate target. We find that generating a −2 OAM order vortex beam requires thicker PhCs than for the −1 OAM order target. Specifically, the optimization of −1 and −2 OAM order vortex beams requires structures with 20 and 30 layers, corresponding to total thicknesses of 2000 nm and 3000 nm, respectively. This trend reflects the crucial role of thickness: thicker structures support more modes, enabling stronger light modulation. Such thickness advantage highlights a key advantage of inverse design, allowing the realization of complex PhCs that exploit multimode interactions to achieve the desired phase and intensity distributions [36]. To further prevent optimization stagnation near singularities (where transmission naturally vanishes) we avoid imposing high target intensities at or near these points. Instead, we sample transmission points along a circle with moderate radius [$0.005(2\pi/a)$ for the −1 OAM order and $0.01(2\pi/a)$ for the −2 OAM order] centered at the singularity, assigning them high target intensities. As optimization proceeds, intensities inside the circle naturally decay to zero. Outside this inner region, we introduce additional concentric circles with gradually larger radii [$0.01(2\pi/a)$ and $0.02(2\pi/a)$ for the −1 OAM order and $0.02(2\pi/a)$ and $0.03(2\pi/a)$ for the −2 OAM order], ensuring a smooth objective function. Beyond producing vortex beams with high purity and uniform phase variation, our inverse design framework can also be extended to realize more complex and unconventional phase/intensity profiles [37].

C. Inverse Design PhCs for Multiplexed Vortex Beam Generation

To further highlight the versatility of our inverse design method, we optimize PhCs for multiplexed vortex beam generation. In designing metasurfaces for functionality multiplexing, the overall optimization target can often be decomposed into smaller tasks, and meta-atoms at different positions are typically designed independently. Each meta-atom only needs to be optimized to produce the desired optical response within its area, which greatly simplifies the design process. However, this approach is not applicable to PhCs. Due to their periodicity, all meta-atoms are identical and are inherently interconnected with each other, as evidenced by their Bloch eigenmodes [38]. Any modification to a part of the PhC's unit cell affects the optical response across the entire momentum space, requiring the whole spectrum to be considered simultaneously. This characteristic removes the need for geometric center alignment, offering unique advantages, but also complicates the design process and hinders the extension of functionalities.

Starting with the −1 OAM order vortex beam, we design PhCs for both polarization-division and momentum-space-division multiplexing, as shown in Fig. 4(a). For polarization-division multiplexing, the PhC is optimized to generate different vortex beams under different incident polarizations. Specifically, it generates a −1 OAM order vortex beam under LCP Gaussian incidence and a −3 OAM order vortex beam under RCP Gaussian incidence. Both vortex beams are generated near the Γ point, which is advantageous for practical applications and relevant to topological photonics, such as skyrmion generation [39]. The result, shown in Fig. 4(b),

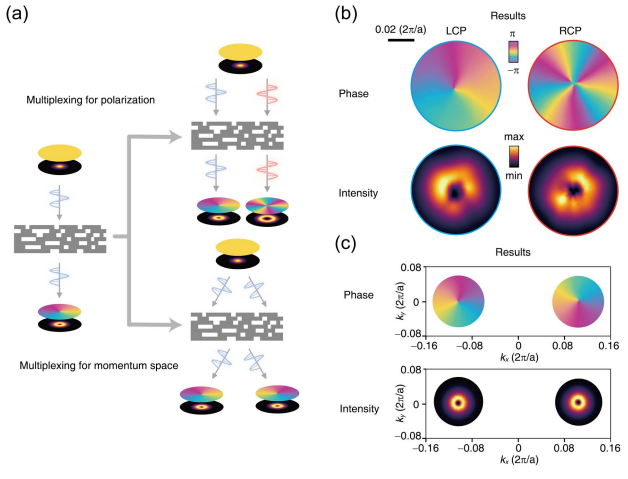

Fig. 4. Inverse design for multiplexed vortex beam generation. (a) Schematic of the polarization-division/momentum-space-division multiplexing. The blue and red color correspond to LCP and RCP light, respectively. Input light with different circular polarization/incident angles can generate vortex beams with different orders. (b) Optimization results for polarization-division multiplexing vortex beam generation. (c) Optimization results for momentum-space-division multiplexing vortex beam generation.

demonstrates desirable phase profiles and high generation efficiencies for both beams. For momentum-space-division multiplexing, different order vortex beams are generated at different momentum-space positions (incident angles) under LCP incidence. The optimized PhC produces a −1 OAM order vortex beam at $k_x = -0.1(2\pi/a)$, $k_y = 0$ and a 1 OAM order vortex beam at $k_x = 0.1(2\pi/a)$, $k_y = 0$, as shown in Fig. 4(c). To maintain computational efficiency, sampling is limited to concentric circles around the two target beams, and only the local phase and intensity profiles are presented. Every intensity profile considers the Gaussian beam incident at the corresponding angle, and desired vortex beams are generated with high efficiency at their required momentum-space positions. This ability to manipulate vortex beams in momentum space provides a powerful tool for exploring the evolution of higher-order vortex beams.

3. CONCLUSIONS

In summary, we propose and implement an inverse design framework for generating high-quality OAM beams with tailored properties in momentum space using PhCs. By integrating backpropagation-based topology optimization with an efficient concentric sampling strategy, our approach enables precise control over polarizations, output angles, and OAM orders. Notably, it allows the realization of both even and odd OAM orders with high-performance, which are difficult to achieve using conventional design approaches. Moreover, we achieve multiplexed vortex beam generations under different polarizations and at distinct momentum-space positions. The results show high purity and efficiency, demonstrating the potential of PhCs as a platform for vortex beam generation and manipulation in momentum space. Such capabilities are particularly promising for future applications in beam shaping [40], on-chip generation [41], and optical trapping [42].

Beyond the demonstrated optical functionalities, our framework also exhibits clear advantages in computational efficiency, scalability, and accuracy. By leveraging gradient information, it efficiently optimizes structures with over 10^5 degrees of freedom, enabling effective exploration of the design space and reliable convergence toward high-performance solutions. It is worth noting that, in addition to the gradient-based approach we employed, numerous other optimization methods exist for the inverse design of photonic structures, such as deep learning and genetic algorithms [43–46]. These alternative approaches warrant further exploration for the inverse design of vortex beam generation in momentum space.

Our work also underscores the critical role of inverse design in producing high-performance PhCs with advanced functionalities, which will be in high demand for future applications and research. This approach is particularly effective for PhCs, where the design is highly complex. While traditional intuition-driven methods are largely limited to simple geometries and high-symmetry designs, inverse design substantially broadens the accessible design space and greatly enhances our ability to tailor PhC properties [21]. We believe that incorporating inverse design into the design paradigm of PhCs will be essential for fully unlocking their potential.

APPENDIX A: PARAMETER SETTINGS AND MATERIAL CONFIGURATION FOR EACH LAYER

The unit cell of our inverse-designed photonic crystal (PhC) is composed of multiple layers of PhC slabs, each 100 nm ($\sim 0.1a$) thick. The number of layers remains fixed during each optimization but is manually adjusted for different design tasks to obtain satisfactory results. Each layer is discretized into a 100×100 voxel grid, with uniform voxel size, and the dielectric constant of each voxel serves as a design parameter. Table 1 lists the parameters used to design the vortex beams with various orbital angular momentum (OAM) presented in this work. Since no symmetry constraints are imposed on the unit cell, the total number of design parameters is determined directly by the voxel count. For example, in the case of −1 OAM order vortex beam, the optimization involves 20 layers and 2×10^5 degrees of freedom.

In our framework, each voxel's design variable, ρ_i, is transformed to the dielectric constant ϵ through a filter-threshold scheme [29]. This scheme consists of a spatial filtering operation followed by a threshold projection, enabling control over feature size and discretization during optimization.

Given the design field $\rho_i \in [0,1]$, filtering operation produces the filtered field $\tilde{\rho}_i \in [0,1]$ by

$$\tilde{\rho}_i = \frac{\sum_{j\in\mathbb{N}_i} \omega(\mathbf{x}_j) v_j \rho_j}{\sum_{j\in\mathbb{N}_i} \omega(\mathbf{x}_j) v_j}, \quad \omega(\mathbf{x}_j) = R - |\mathbf{x}_i - \mathbf{x}_j|,$$

where v_j is the volume of the element j, and $\omega(\mathbf{x}_j)$ is the weighting function that takes neighboring elements in radius R into consideration. This operation smooths the design field ρ_i, and the radius R effectively controls the minimum feature size. Since this process is fully differentiable, it can be implemented using automatic differentiation to compute gradients via backpropagation.

Table 1. List of Parameters for Designing Vortex Beams with Different OAM Orders

OAM Order	Multiplexing Scheme	Polarization State	Layer Number	Degrees of Freedom
−1	N.A.	Co-polarization	20	2×10^5
−2	N.A.	Co-polarization	30	3×10^5
−1	N.A.	Cross-polarization	20	2×10^5
−2	N.A.	Cross-polarization	30	3×10^5
−3, −1	Polarization-division	Co-polarization	40	4×10^5
−1, 1	Momentum-space-division	Co-polarization	30	3×10^5

Given the filtered field $\tilde{\rho}_i \in [0,1]$, threshold projection produces the physical field $\bar{\rho}_i \in [0,1]$ by

$$\bar{\rho}_i = \frac{\tanh(\beta \cdot \eta) + \tanh(\beta \cdot (\tilde{\rho}_i - \eta))}{\tanh(\beta \cdot \eta) + \tanh(\beta \cdot (1.0 - \eta))}.$$

This function serves as a differentiable approximation of the Heaviside function, where η denotes the threshold value, and β controls the steepness of the transition. It drives values greater than η toward 1 and values smaller than η toward 0. Finally, the physical field $\bar{\rho}_i$ is related to the dielectric constant ϵ as follows:

$$\epsilon_i = \epsilon_{\min} + \bar{\rho}_i(\epsilon_{\max} - \epsilon_{\min}),$$

where $\epsilon_{\min}$ and $\epsilon_{\max}$ denote the dielectric constants of the void and the solid structure, respectively. Initially, β is set to a small value, allowing all design parameters to vary freely and fully explore the entire parameter space (continuous phase). As the optimization proceeds, the value of β is gradually increased, which progressively enforces the binarization of the physical field $\bar{\rho}_i$, a requirement for practical fabrication (discretization phase).

APPENDIX B: VORTEX BEAM GENERATION UNDER CROSS-POLARIZATION

In the main text, we have optimized co-polarized vortex beams with both even and odd OAM orders. Here, we further optimize vortex beams with −1 and −2 OAM orders under cross-polarization at 780 nm to demonstrate the capability and versatility of our method. The structures consist of 20 and 30 layers for the −1 and −2 OAM order beams, respectively. Each layer is 100 nm ($\sim 0.1a$) thick and discretized into a 100×100 voxel grid, where each voxel is either void ($\epsilon = 1$) or solid ($\epsilon = 3$). Ninety sampling points are used to construct the final FoM, and the discretization schedule follows the same settings as in the previous optimizations (100 iterations for the continuous phase and 400 iterations for the discretization phase). It is found that enlarging the radii of the sampling circles is necessary for achieving successful optimization under cross-polarization, with radii of $0.02(2\pi/a)$, $0.03(2\pi/a)$, and $0.04(2\pi/a)$ for both the −1 and −2 OAM orders. The optimization results are shown in Fig. 5, and vortex beams with both even and odd OAM orders can be generated with high efficiency and purity.

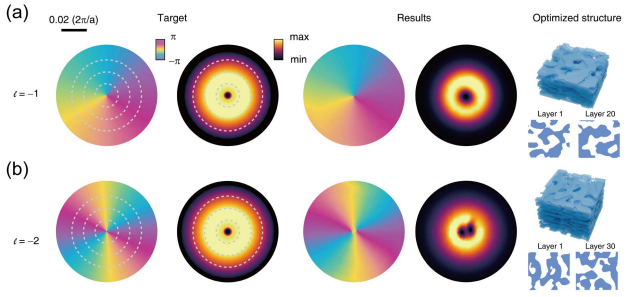

Fig. 5. Inverse-designed vortex beam with different orders under cross-polarization. (a) The optimization target and results for the −1 OAM order vortex beam. (b) The optimization target and results for the −2 OAM order vortex beam.

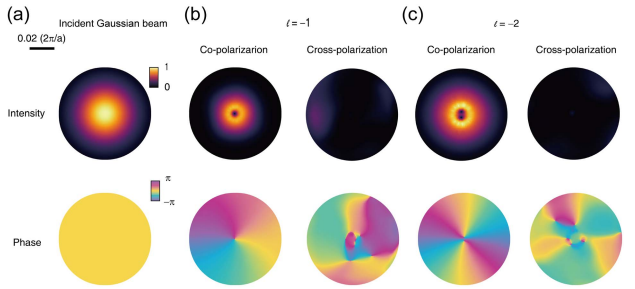

Fig. 6. Co- and cross-polarization fields of inverse-designed photonic crystals that generate vortex beams with different orders under co-polarization. (a) The intensity and phase profiles for the incident Gaussian beam. (b) Unnormalized co- and cross-polarization fields for the −1 OAM order vortex beam. (c) Unnormalized co- and cross-polarization fields for the −2 OAM order vortex beam.

APPENDIX C: FIELD DISTRIBUTIONS UNDER CROSS-POLARIZATION

In previous studies, OAM beam generation in PhCs typically relies on topological polarization vortices in momentum space, and the OAM order is closely related with the polarization modes [17,18]. Based on a polarization vortex with topological charge q, a vortex beam with OAM order $|l| = 2q$ can be produced through the geometric phase under cross-polarization, while the co-polarized component retains a Gaussian profile without phase singularities. To examine whether a similar phenomenon exists in our optimized results, we present the phase and intensity distributions for both co- and cross-polarization for the inverse-design PhCs under co-polarization, as shown in Figs. 6(b) and 6(c). The corresponding incident Gaussian beam profile is provided in Fig. 6(a). The intensity under cross-polarization is not normalized to clearly display the field contrast. We do not observe a clear correlation between the OAM orders of the co- and cross-polarization modes. Since the vortex beams generated under co-polarization exhibit very high efficiency, the corresponding intensity under cross-polarization is nearly zero. Multiple phase singularities appear in the cross-polarized field, making it difficult to define an OAM order for the entire beam.

APPENDIX D: PURITY ANALYSIS FOR THE GENERATED VORTEX BEAMS

Here, we consider the decomposition based on Laguerre–Gaussian (LG) modes. The directly transmitted electric field in momentum space $E(k,\phi)$ can be expressed in a set of orthogonal LG modes as

$$E(k,\phi) = \sum_{p,l} C_{p,l} \mathrm{LG}_{p,l}(k,\phi),$$

where $C_{p,l}$ is the complex correlation coefficient representing the contributions of each basis mode $\mathrm{LG}_{p,l}$. The LG basis at the beam waist ($w = w_0$) can be expressed as

$$\mathrm{LG}_{p,l}(k,\phi) = \sqrt{\frac{2p!}{\pi w_0^2 (p+|l|)!}} \left(\frac{k\sqrt{2}}{w_0}\right)^{|l|} L_p^{|l|}\left(\frac{2k^2}{w_0^2}\right) e^{-\frac{k^2}{w_0^2}} e^{-il\phi}.$$

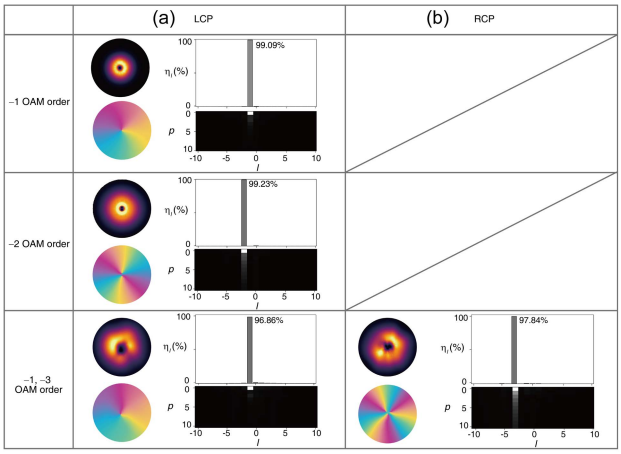

Fig. 7. OAM mode purity analysis for vortex beams generated from inverse-designed photonic crystals. (a) The OAM mode purity analysis for vortex beams with left-handed circular polarization. (b) The OAM mode purity analysis for vortex beams with right-handed circular polarization.

Here, (k, ϕ) are the radial and azimuthal coordinates in the transverse plane, l is the OAM index, $p \geq 0$ is the radial index determining the number of radial nodes in the intensity distribution, and $L_p^{|l|}(x)$ is the associated Laguerre polynomial of orders p, l. The OAM purity is obtained by evaluating the mode weightings $|C_{l,p}|^2$, where each coefficient is computed through the inner product,

$$C_{p,l} = \langle \mathrm{LG}_{p,l}(k,\phi)|E(k,\phi)\rangle = \iint_{R^2} \mathrm{LG}^*_{p,l}(k,\phi)E(k,\phi)\mathrm{d}^2k.$$

Then, the purity (η^n) corresponding to the OAM order $l = n$ is then obtained by

$$\eta^n = \frac{|C_n|^2}{\sum_l |C_l|^2}, \quad |C_l|^2 = \sum_p |C_{p,l}|^2.$$

The calculated mode purities (η^n) and mode weightings $|C_{l,p}|^2$ for our results are shown in Figure 7. All the optimized vortex beams with various OAM orders exhibit near-unity mode purity, demonstrating the strong capability of our proposed framework.

Funding. National Key Research and Development Program of China (2023YFA1406900, 2022YFA1404800); National Natural Science Foundation of China (12234007, 12321161645, 12221004, 12404427, T2394480, T2394481); Science and Technology Commission of Shanghai Municipality (24YF2702400, 22142200400, 21DZ1101500, 2019SHZDZX01, 23DZ2260100).

Acknowledgment. The authors acknowledge useful comments and suggestions received from Professor Cheng-Wei Qiu and Dr. Xiaobin Lin.

Disclosures. The authors declare no conflicts of interest.

Data Availability. Data underlying the results presented in this paper are not publicly available at this time but may be obtained from the authors upon reasonable request.

REFERENCES

1. P. Coullet, L. Gil, and F. Rocca, "Optical vortices," Opt. Commun. **73**, 403–408 (1989).
2. J. Wang, "Advances in communications using optical vortices," Photonics Res. **4**, B14–B28 (2016).
3. A. E. Willner, H. Huang, Y. Yan, *et al.*, "Optical communications using orbital angular momentum beams," Adv. Opt. Photonics **7**, 66–106 (2015).
4. S. Fürhapter, A. Jesacher, S. Bernet, *et al.*, "Spiral phase contrast imaging in microscopy," Opt. Express **13**, 689–694 (2005).
5. R. Zheng, R. Pan, G. Geng, *et al.*, "Active multiband varifocal metalenses based on orbital angular momentum division multiplexing," Nat. Commun. **13**, 4292 (2022).
6. A. Mair, A. Vaziri, G. Weihs, *et al.*, "Entanglement of the orbital angular momentum states of photons," Nature **412**, 313–316 (2001).
7. C. Li, J. Jang, T. Badloe, *et al.*, "Arbitrarily structured quantum emission with a multifunctional metalens," eLight **3**, 19 (2023).
8. M. Berry and W. Liu, "No general relation between phase vortices and orbital angular momentum," J. Phys. A **55**, 374001 (2022).
9. A. M. Yao and M. J. Padgett, "Orbital angular momentum: origins, behavior and applications," Adv. Opt. Photonics **3**, 161–204 (2011).
10. Y. Shen, X. Wang, Z. Xie, *et al.*, "Optical vortices 30 years on: OAM manipulation from topological charge to multiple singularities," Light Sci. Appl. **8**, 90 (2019).
11. X. Wang, Z. Nie, Y. Liang, *et al.*, "Recent advances on optical vortex generation," Nanophotonics **7**, 1533–1556 (2018).
12. A. Mourka, J. Baumgartl, C. Shanor, *et al.*, "Visualization of the birth of an optical vortex using diffraction from a triangular aperture," Opt. Express **19**, 5760–5771 (2011).
13. K. Sueda, G. Miyaji, N. Miyanaga, *et al.*, "Laguerre-Gaussian beam generated with a multilevel spiral phase plate for high intensity laser pulses," Opt. Express **12**, 3548–3553 (2004).
14. F. Cardano, E. Karimi, S. Slussarenko, *et al.*, "Polarization pattern of vector vortex beams generated by *Q*-plates with different topological charges," Appl. Opt. **51**, C1–C6 (2012).
15. F. Yue, D. Wen, J. Xin, *et al.*, "Vector vortex beam generation with a single plasmonic metasurface," ACS Photonics **3**, 1558–1563 (2016).
16. Z. Jin, D. Janoschka, J. Deng, *et al.*, "Phyllotaxis-inspired nanosieves with multiplexed orbital angular momentum," eLight **1**, 5 (2021).
17. B. Wang, W. Liu, M. Zhao, *et al.*, "Generating optical vortex beams by momentum-space polarization vortices centred at bound states in the continuum," Nat. Photonics **14**, 623–628 (2020).
18. T. Li, J. Wang, W. Zhang, *et al.*, "High-efficiency nonlocal reflection-type vortex beam generation based on bound states in the continuum," Natl. Sci. Rev. **10**, nwac234 (2023).
19. W. Liu, L. Shi, J. Zi, *et al.*, "Ways to achieve efficient non-local vortex beam generation," Nanophotonics **10**, 4297–4304 (2021).
20. S. Molesky, Z. Lin, A. Y. Piggott, *et al.*, "Inverse design in nanophotonics," Nat. Photonics **12**, 659–670 (2018).
21. R. Deng, W. Liu, and L. Shi, "Inverse design in photonic crystals," Nanophotonics **13**, 1219–1237 (2024).
22. C. M. Lalau-Keraly, S. Bhargava, O. D. Miller, *et al.*, "Adjoint shape optimization applied to electromagnetic design," Opt. Express **21**, 21693–21701 (2013).
23. M. Minkov, I. A. Williamson, L. C. Andreani, *et al.*, "Inverse design of photonic crystals through automatic differentiation," ACS Photonics **7**, 1729–1741 (2020).
24. C. Xiao, M. Liu, K. Yao, *et al.*, "Ultrabroadband and band-selective thermal meta-emitters by machine learning," Nature **643**, 80–88 (2025).
25. H. Wang, W. Jin, C. Guo, *et al.*, "Design of compact meta-crystal slab for general optical convolution," ACS Photonics **9**, 1358–1365 (2022).
26. R. Deng, X. Wang, Y. Zuo, *et al.*, "Broadband complete polarization control via inverse-designed photonic crystal slabs," Adv. Opt. Mater. **12**, 2303218 (2024).

27. O. Sigmund and K. Hougaard, "Geometric properties of optimal photonic crystals," Phys. Rev. Lett. **100**, 153904 (2008).
28. J. S. Jensen and O. Sigmund, "Topology optimization for nano-photonics," Laser Photonics Rev. **5**, 308–321 (2011).
29. F. Wang, B. S. Lazarov, and O. Sigmund, "On projection methods, convergence and robust formulations in topology optimization," Struct. Multidiscip. Optim. **43**, 767–784 (2011).
30. Y. LeCun, Y. Bengio, and G. Hinton, "Deep learning," Nature **521**, 436–444 (2015).
31. D. Maclaurin, D. Duvenaud, and R. P. Adams, "Autograd: effortless gradients in Numpy," in *ICML AutoML Workshop (CNRS)* (2015), pp. 1–3.
32. W. Jin, W. Li, M. Orenstein, *et al.*, "Inverse design of lightweight broadband reflector for relativistic lightsail propulsion," ACS Photonics **7**, 2350–2355 (2020).
33. C. Zhu, R. H. Byrd, P. Lu, *et al.*, "Algorithm 778: L-BFGS-B: Fortran subroutines for large-scale bound-constrained optimization," ACM Trans. Math. Softw. **23**, 550–560 (1997).
34. C. Han, J. He, C. Tong, *et al.*, "Generating first-order optical vortex beams by photonic crystal slabs," Opt. Express **32**, 27591–27598 (2024).
35. B. Zhen, C. W. Hsu, L. Lu, *et al.*, "Topological nature of optical bound states in the continuum," Phys. Rev. Lett. **113**, 257401 (2014).
36. D. A. Miller, "Why optics needs thickness," Science **379**, 41–45 (2023).
37. Z. Yu, X. Gao, J. Yao, *et al.*, "A spatial-frequency patching metasurface enabling super-capacity perfect vector vortex beams," eLight **4**, 21 (2024).
38. J. D. Joannopoulos, S. G. Johnson, J. N. Winn, *et al.*, *Photonic Crystals: Molding the Flow of Light*, 2nd ed. (Princeton University, 2008).
39. L. Rao, J. Wang, X. Wang, *et al.*, "Meron spin textures in momentum space spawning from bound states in the continuum," Phys. Rev. Lett. **135**, 026203 (2025).
40. W. Lee, X.-C. Yuan, and W. Cheong, "Optical vortex beam shaping by use of highly efficient irregular spiral phase plates for optical micromanipulation," Opt. Lett. **29**, 1796–1798 (2004).
41. H. Huang, A. C. Overvig, Y. Xu, *et al.*, "Leaky-wave metasurfaces for integrated photonics," Nat. Nanotechnol. **18**, 580–588 (2023).
42. D. G. Grier, "A revolution in optical manipulation," Nature **424**, 810–816 (2003).
43. P. R. Wiecha, A. Arbouet, C. Girard, *et al.*, "Deep learning in nano-photonics: inverse design and beyond," Photonics Res. **9**, B182–B200 (2021).
44. W.-L. Hsu, C.-Y. Yu, Y.-S. Huang, *et al.*, "Simplest but efficient design of a color router optimized by genetic algorithms," ACS Photonics **12**, 1402–1408 (2025).
45. G. Wu, L. Si, H. Xu, *et al.*, "Phase-to-pattern inverse design for a fast realization of a functional metasurface by combining a deep neural network and a genetic algorithm," Opt. Express **30**, 45612–45623 (2022).
46. N. Omrani, F. Ghorbani, S. Beyraghi, *et al.*, "Deep learning design of orbital angular momentum generators by leaky-wave holograms," IEEE Antennas Wireless Propag. Lett. **23**, 264–268 (2023).